CYCLE II.5

AIRCRAFT AERO-OPTICAL TURBULENT BOUNDARY-LAYER/SHEAR-LAYER MEASUREMENTS

K. Gilbert

Introduction

The Air Force Weapons Laboratory (AFWL) has completed a series of airborne laser propagation through aircraft turbulent boundary layers and shear layers. These airborne tests, in a sense, are the culmination of a 3-year program at AFWL to investigate aircraft viscous airflow effects. The primary objective was to make two independent assessments of optical performance through these random flows. The first is an integrated path optical measurement using a Fast Shearing Interferometer (FSI). The second technique involves inferring point measurements of unsteady densities and correlation lengths within the flows. This in turn leads to optical degradation predictions via the Gladstone-Dale law. By integrating along these points, one then obtains an independent prediction of net optical degradation. The purpose of this paper is to summarize these data vis-a-vis future airborne laser weapon systems.

Optical instrumentation included a Fast Shearing Interferometer (FSI) developed by Lincoln Laboratory, together with a helium-neon laser source. The 9-cm collimated laser beam made a double pass through the aircraft boundary layer via reflection from an airfoil mirror located about 1 meter from the fuselage. Averaging a large number of Modulation Transfer Functions (MTFs) for a particular aircraft condition and Fourier transforming this average yields the expected far-field intensity degradation for an aircraft-mounted laser system.

Aerodynamic measurements within the boundary layer included fine wire probes to measure temperature and mass flux fluctuations. A laser Doppler velocimeter employed a 5-watt argon-ion laser to measure unsteady velocity. This, in turn, leads to optical degradation predictions via the Gladstone-Dale law. The aerodynamic equipment was developed largely by NASA Ames. In addition, an array of thermocouples was attached to the skin of the aircraft to measure heat transfer between the cabin and the external flow. This is a parameter critical to the understanding of the source of density fluctuations within the aircraft boundary layer.

The 13-flight measurement program examined fundamental aero-optical properties of fuselage turbulent boundary layers and shear layers (the latter formed via a fence sans cavity arrangement.) The experimental setup and instrumentation employed were analogous to previous wind tunnel tests and are shown in Figure 1. Altitudes ranged from 0.3 km to 11.3 km while Mach numbers varied from 0.25 to 0.85. Two fences, located in two positions relative to the optical axis, were examined.

The hot-wire anemometer and laser Doppler velocimeter probes could be moved continuously through the aircraft random flow regions and into the free stream. By making certain assumptions, including the neglect of total temperature and pressure fluctuations in the flow, the fluid unsteady density (ρ') and its correlation length in the propagation direction (ℓ_z) could be inferred at a series of points from the fuselage skin out into the free stream. Integrating along this path, one can obtain an estimate of the Strehl ratio I/I_0 from the relation (ref. 1)

$$\frac{I}{I_o} = e^{-\sigma^2 K^2} \qquad (1)$$

where

$$K = \frac{2\pi}{\lambda} \qquad (2)$$

$$\sigma^2 = \sqrt{\pi} \quad \beta^2 \qquad \int_0^L \langle \rho' \rangle^2 \, \ell_z \, dz \qquad (3)$$

β = Gladstone-Dale constant

L = Thickness of random flow region

Note the expression for the rms phase variance in equation 1 assumes a Gaussian correlation function. However, the data were found to be more closely fit by an exponential correlation function. In this case, a multiplicative factor of two replaces π in the above expression for σ. The assumption of an exponential correlation function will be assumed herein. A large aperture is an implicit assumption in equation 1 ($D >> \ell_z$). Details of these aero measurements appear elsewhere (ref. 2).

A direct and independent estimate of this Strehl ratio I/I_o is afforded by the integrated path double pass MTF measurement. By averaging approximately 250 of this tilt-insensitive MTFs and then Fourier transforming this average, a prediction of far-field degradation is obtained. However, to provide a direct comparison with the aero prediction (equation 1), a correction for the experimental noninfinite aperture MTF (i.e., $D \not\gg \ell_z$) must be applied. This follows by taking the general expression for tilt-insensitive MTF (ref. 3).

$$\tau \left(s, \frac{D}{\ell_z} \right) = M_a \, e^{-\sigma^2} \left[1 - e^{-\left(Ds/2\ell_z \right)^2} \right] \qquad (4)$$

where

M_a = MTF of optics

σ^2 = rms phase variance

D = telescope aperture diameter

s - shear frequency, $0 \leq s \leq 2$

and integrating under τ for several values of σ and D/ℓ_Z. A Strehl family of curves (Figure 2) is obtained. From the measured value of ℓ_Z, one can then obtain an infinite aperture Strehl value. Then the average value of ℓ_Z from the aerodynamic measurements, together with the empirical value of I/I_0, yields an estimate of the infinite aperture Strehl value. We now turn to a discussion of the aero-optical data.

Turbulent Boundary Layer Data

Figure 3 shows a sampling of unsteady density profiles following from hot-wire anemometer and laser Doppler velocimeter turbulent boundary layer measurements. Figure 4 shows the corresponding correlation lengths measured in the direction of propagation.

A summary of this turbulent boundary layer data appears in Table 1. Columns 1 through 3 show the aircraft parameters of altitude, Mach number, and dynamic pressure, respectively. Column 4 lists the average correlation lengths in the propagation direction, while column 5 depicts the approximate boundary layer thicknesses. The maximum unsteady density is shown in column 6, with ρ_∞ being the free stream value of density. The measured (MTF) integrated path Strehl ratio appears in column 7, here corrected to represent a single pass through the boundary layer. Column 8 lists the extrapolated optical Strehl for an infinite aperture ($D >> \bar{\ell}_Z$), using Figure 2. The adjacent column 9 shows the corresponding Strehl number predicted from the unsteady density and correlation length profiles, using equation 1. In columns 7 and 9 the errors shown are rms values associated with the several aerodynamic or optical measurements at that test point. The final column represents the rms phase variance in units of HeNe (λ 0.63 μm) wavelength following from the aerodynamic Strehl prediction, $(I/I_0)_A$. A correlation plot of the aerodynamically and optically inferred values of I/I_0 appears in Figure 5.

Table 1

BOUNDARY LAYER DATA

A(km)	M	q	$\overline{\ell}_z$(cm)	L(cm)	$\frac{\rho' \max}{\rho_\infty}$	$(I/I_0)_{OPT}$	$(I/I_0)_{\infty\,OPT}$	$(I/I_0)_A$	$\sigma(\lambda)$
0.3	0.25	0.04	1.1	25	0.13	0.80±0.11	0.73	0.77	0.081
3.3	0.35	0.06	1.8	29	0.22	0.85±0.04	0.78	0.69	0.097
10.7	0.57	0.07	3.3	32	0.47	0.75±0.06	0.50	0.64±0.01	0.106
7.6	0.57	0.10	2.6	30	0.42	0.65±0.10	0.44	0.61±0.02	0.112
5.5	0.57	0.12	2.6	32	0.46	0.57±0.09	0.32	0.54±0.10	0.125
3.8	0.57	0.15	1.9	34	0.41	0.63±0.10	0.46	0.54±0.01	0.125
1.2	0.57	0.19	3.4	33	0.49	0.62±0.10	0.30	0.27	0.182

Shear Layer Data

Two fences, each mounted flush with the aircraft fuselage, were examined in this test series. Both were 14.5 cm in height and 48 percent porosity. The near fence (F_s) was mounted 8 cm upstream of the optical axis, while its counterpart (F_m) was located 80 cm upstream. The fences had hole diameters of 0.7 mm. Each fence had a smooth top edge.

Figure 6 shows unsteady density profiles for two cases representative of the near fence (F_s) and middle fence (F_m) data base. Again the $z = 0$ intercept corresponds with the aircraft fuselage. Notice the shear layer thickness for the near fence (F_s) is of the order of a few centimeters, while that for (F_m) is approximately 25 cm. Average density correlation lengths in the z-direction ($\overline{\ell}_z$) lengths range from a sizable fraction of the F_s shear thickness to about 1/20th of the F_m shear layer breadth. These are shown in Figure 7. In general, the average correlation lengths are considerably smaller than those for corresponding boundary layer conditions, while the unsteady density strength is somewhat greater.

Table 2 is a synopsis of the fence data. The columns here are defined as in Table 1. Again, the optical MTF infinite aperture Strehl number (column 9) is obtained using Figure 2 and the measured value of $\overline{\ell}_z$. Errors

Table 2

SUMMARY OF FENCE DATA

A(km)	q	M	L(cm)	$\overline{\ell}_z$	$\frac{\rho'_{max}}{\rho_\infty}$	$(I/I_0)_{OPT}$	$(I/I_0)_{\infty OPT}$	$(I/I_0)_A$	$\sigma(\lambda)$
Configuration F_s									
0.30	0.04	0.25	30	1.1	0.4	0.77	0.69	0.73	0.089
11.3	0.06	0.57	34	2.1	1.2	0.71	0.55	0.70	0.095
7.6	0.10	0.57	32	1.3	1.3	0.64	0.50	0.49	0.134
5.5	0.12	0.57	34	1.4	1.0	0.57	0.42	0.41	0.148
1.2	0.19	0.57	33	0.9	2.6	0.48	0.33	0.07	0.260
Configuration F_m									
0.30	0.04	0.25	35	0.9	0.2	0.84	0.80	0.76	0.083
10.7	0.06	0.57	35	1.3	0.8	0.72	0.59	0.70	0.095
7.6	0.10	0.57	35	1.2	0.8	0.66	0.54	0.61	0.112
5.5	0.12	0.57	35	1.2	0.9	0.64	0.51	0.46	0.140
1.2	0.19	0.57	35	0.9	1.0	0.59	0.36	0.26	0.185

are not specified in this table. However, both the aero and optical data were more consistent than the turbulent boundary layer results. In no case did the variation among multiple measurements for a given test point exceed 5 percent. Again, a correlation plot of the aerodynamic and optical Strehl values appears in Figure 8.

Discussion

Correlations between the integrated path MTF optical measurement ($D >> \bar{\ell}_z$) and the aerodynamically inferred Strehl value (assuming an exponential density correlation function) are, in general, very good. The rms phase variances, calculated from the aerodynamic Strehl ratios, ranged from 0.08 to 0.18 HeNe (λ = 0.63 μm) waves over an aircraft dynamic pressure variation of 0.04 to 0.19 (standard) atmospheres.

The fence shear layer data were very self-consistent. The free shear formed at the top edge of the fences contained the expected smaller correlation lengths than corresponding fuselage boundary layers. However, the strength of the fluctuating density component was greater. Since the rms phase variance scales approximately as $\ell_z \overline{<\rho'>^2}$, the result was a greater observed optical degradation in shear layers. In general, the rms phase variance ranged from 0.09 to 0.26, and 0.08 to 0.19 for the near fence (F_s) and middle fence (F_m), respectively (same q variation as boundary layer). Another interesting facet of the fences was the nearly equal levels of optical degradation observed for F_s and F_m under the same flight conditions. To first approximation, it appears that optical seeing behind a fence is independent of the downstream location of the optical axis.

The results of the fuselage heat flux measurements were detailed in an earlier article (ref. 4). It was found that varying cabin temperatures from 9° to 40°C had negligible effect on either the aerodynamically inferred unsteady density profiles on the optical MTF (I/I_0) measurements. The aircraft skin appears to act as an adiabatic wall vis-a-vis turbulent boundary layers and shear layers.

Because tomorrow's airborne laser systems may operate across a broad spectrum of wavelengths, telescope diameters, and aircraft conditions, it is essential to detail scaling laws for the data.

Wavelength Scaling

A previous article (ref. 5) has discussed implications of the present data base for short wavelength lasers. Again, in the infinite aperture limit ($D \gg \overline{\ell}_z$), wavelength (λ) scaling is in accordance with equation 1, which we rewrite here as

$$I/I_0 = e^{-(2\pi\sigma/\lambda)^2} \qquad (5)$$

Figure 9 shows the dependence of Strehl ratio on λ, using the largest q values from Tables 1 and 2 (i.e., altitude 1.2 km, Mach #0.57). Shown in each case are both the infinite aperture optical MTF result and the aerodynamic prediction of I/I_0. The thick boundary layer (33 cm) in this case renders these results rather conservative; nevertheless, it is seen that the fuselage viscous flow field will probably be an important source of laser optical degradation for $\lambda \lesssim 2$ μm. Moreover, fence effects associated with windowless turret operation are essentially independent of boundary layer thickness (ref. 6) and hence location on the aircraft. Shear layer-induced far-field degradation is likely to be the dominant error source for short wavelength ($\lambda \lesssim 2$ μm) airborne laser systems.

Aperture Scaling

Experiments (ref. 1) have shown that for a constant average density correlation length $\overline{\ell}_z$, the variation of far-field intensity (Strehl ratio) with aperture size closely follows the family of curves depicted in Figure 2, both for shear layers and for natural aircraft boundary layers. Thus, from MTF measurements for several aperture diameters, one can infer the Strehl ratio I/I_0, and hence estimate the rms phase variance σ. In the infinite aperture limit, equation 1 applies.

Turbulent Boundary Layer Thickness Scaling

Scaling with boundary thickness L has been found to go approximately as (ref. 2)

$$\frac{I}{I_0} = e^{-c\ (KL^{2/3})^{3}} \qquad (6)$$

where

$K = 2\pi/\lambda$

c is a constant

Figure 10 shows the dependence of far-field intensity degradation on L, again using the boundary layer high q value of $(I/I_0)_A$ as a baseline, and assuming $\lambda = 0.63$ µm. Clearly, to minimize boundary layer optical degradation, the airborne laser telescope should be placed as far forward as possible on the aircraft.

Scaling with Aircraft q

Tables 1 and 2 show that, in general, optical degradation increases as the aircraft dynamic pressure increases. Figure 11 shows this dependence for both boundary layer and fence data. Here, dimensionless rms phase variance $(\overset{*}{\sigma}^2)$ plots against aircraft dynamic pressure q indicate a reasonably good correlation between these two parameters.

Conclusions

Aero-optical properties of aircraft turbulent boundary layers and fence-induced shear layers have been examined for altitudes up to 12 kilometers and Mach numbers extending into the high transonic region. Aerodynamic instrumentation included movable hot-wire anemometer probes and a laser Doppler velocimeter, enabling point measurements of fluctuating density strengths and correlation lengths within the random flow region. Integration across the layer then leads to an estimate of the rms optical phase variance and, hence, the Strehl ratio (I/I_0) for a laser beam traversing the region.

An independent optical MTF measurement was performed in autocollimation using a 9-cm diameter helium-neon laser and a reflective airfoil located in the free stream. By averaging a large number of MTFs, Fourier transforming, and correcting for a single pass through the boundary layer, an optical assessment of I/I_0 was obtained. An array of thermocouples was also attached to the inside skin of the aircraft to examine the prevalent adiabatic wall assumptions vis-a-vis boundary layers. The principal conclusions from these aircraft tests include the following.

1. Correlations between the turbulent boundary layer (TBL) aerodynamically inferred Strehl ratio $(I/I_0)_A$ and its MTF optical counterpart $(I/I_0)_{OPT}$ (the latter corrected for large aperture) were good. The RMS phase variance was observed to increase from 0.08 to 0.18 wave (λ = 0.63 μm) for aircraft dynamic pressures q ranging from 0.04 to 0.19 standard atmosphere.

2. Measured TBL density correlation lengths varied from about 1.0 to 3.5 cm, representing 5 to 10 percent of the total boundary layer thickness. The correlation functions themselves appear to be exponential.

3. Maximum TBL unsteady density strength $(\rho'/\rho_\infty)_{max}$ was of order 0.5 percent over the experimental range of aircraft dynamic pressures.

4. The aircraft skin appears to act as an adiabatic wall. Neither the aerodynamic probes nor the integrated path MTF measurements showed appreciable evidence of heat transport between the fuselage and the TBL.

5. A strong shear layer (SL) is formed at the top edge of an aerodynamic fence. Measured correlation lengths are generally smaller (1 to 1.5 cm) than for TBLs, though the strength of the turbulence is significantly greater (0.5 to 3 percent). Most of the total path optical degradation is produced within the SL itself.

6. Identical fences (no cavity) were examined for two locations--8 and 80 cm upstream of the optical axis; to first order, the observed optical degradations were the same for the two locations for equal values. This indicates that optical degradation is essentially independent of fence location within this experimental domain.

7. For both the near fence (F_s) and the middle fence (F_m), sound correlations were observed between the aero Strehl prediction $(I/I_0)_A$ and the optical measurement. An exception is for the highest q values. The reason for this discrepancy is not understood. Inferred rms phase variances for F_s and F_m were 0.09 to 0.26 and 0.08 to 0.19 wave (λ = 0.63 μm), respectively.

8. The experiments involved a single wavelength (λ=0.63 μm), one MTF aperture diameter (9 cm), and a single location on the aircraft fuselage (station 25 meters). Clearly it is crucial to understand the scaling of this data base for other airborne laser conditions. Previous AFWL wind tunnel and aircraft experiments have established these relationships. We now detail these.

a. Aperture Scaling. Operational airborne laser weapon systems will probably have telescope diameters which are large compared with fuselage random flow-field density correlation lengths (i.e., $D \gg \ell_z$). This condition did not prevail. Thus, a correction was applied to the optical data, using an expansion for the tilt-removed MTF, which has been verified in wind tunnel experiments. The magnitude of the correction for the data varied from about 5 to 50 percent.

b. Wavelength Scaling. For a large aperture system, wavelength scaling follows from the established relationship

$$\frac{I}{I_0} = e^{-K^2\sigma^2} \tag{7}$$

with

$K = 2\pi/\lambda$ (wave vector)

σ = RMS phase variance

Notice the strong sensitivity of Strehl ratio with wavelength; indications are that airborne systems employing lasers with wavelengths less than 2 μm can expect moderate-to-strong optical degradation due to turbulent boundary layers and severe effects from SLs.

c. Scaling with Boundary Layer Thickness. Fence-induced optical effects are essentially independent of turbulent boundary layer thickness. Rather, the strong shear layer formed at the top edge of the fence dominates. In the case of a pure boundary layer, however, as might exist for a flush-mounted turret with an exit material window, the $_{rms}$ phase variance has been found to scale roughly as

$$\sigma^2 \propto L^{4/3} \tag{8}$$

where L is the thickness of the random domain. It clearly behooves one to install this turret as far forward on the aircraft as possible.

d. Scaling with Aircraft Dynamic Pressure q. For both the fence (shear layer) results and the natural aircraft boundary layer, the phase variance is roughly proportional to q.

9. The results established the relevancy of previous wind tunnel experiments. Fluctuating density strengths and correlation lengths are in general agreement, both for the artificially thickened wind tunnel boundary layers and shear layers. These latter were examined both in a cavity-fence and a cavity-mass injection configuration. Though anomalies exist, the general conclusion is that the random flow fields created in wind tunnels have the same general characteristics as those observed in the airborne experiments.

10. Near-term adaptive optics systems will be unable to cope with boundary layers and shear layers due to their small spatial and large bandwidth requirements.

11. Aircraft random flow fuselage effects in the transonic region are not an important source of laser optical degradation for wavelengths in the middle IR region ($\lambda \gtrsim 2$ μm). However, as the evolution of shorter wavelength systems continues, the importance of these aircraft effects will assume major dimensions. This present data base suggests the following guidelines for developing short wavelength airborne laser systems.

a. Operate the laser turret closed port (i.e., window) if possible; flush mount to preclude formation of shear layers.

b. Place the turret as far forward as possible to minimize boundary layer thickness.

If windowless turret operation is required, or look angle requirements lead to propagation through a shear layer, the resultant degradation could be stifling. Support research aimed at diverting, suctioning, or otherwise ameliorating the effects of random flow fields on short wavelength systems, in the long run may be a key to the successful evolution of these future airborne weapon systems.

REFERENCES

1. Gilbert, K. G., et al., Laser Propagation Through Turbulent Boundary Layers, Shear Layers and Cavity Flows: Wind Tunnel Experiments, Laser Digest, AFWL-TR-78-15, 1978.
2. Rose, W., Aerodynamic Measurements of KC-135 Turbulent Boundary Layers, NASA CP-2121, 1980.
3. Barakat, R., OPT. ACTA, 18, 683 (1971).
4. Gilbert, L., Cycle II.5 Thermo-Optical Turbulent Boundary Layer Measurements, Laser Digest, AFWL-TR-78-15, 1978.
5. Gilbert, K., Implications of Recent Aircraft Random Flow Field Experiments for Short Wavelength Laser Systems, Laser Digest, AFWL-TR-78-15, 1978.
6. Gilbert, K., Open Port Laser Turret Optical Performance: Recent Experiments, Laser Digest, AFWL TR-78-15, 1978.

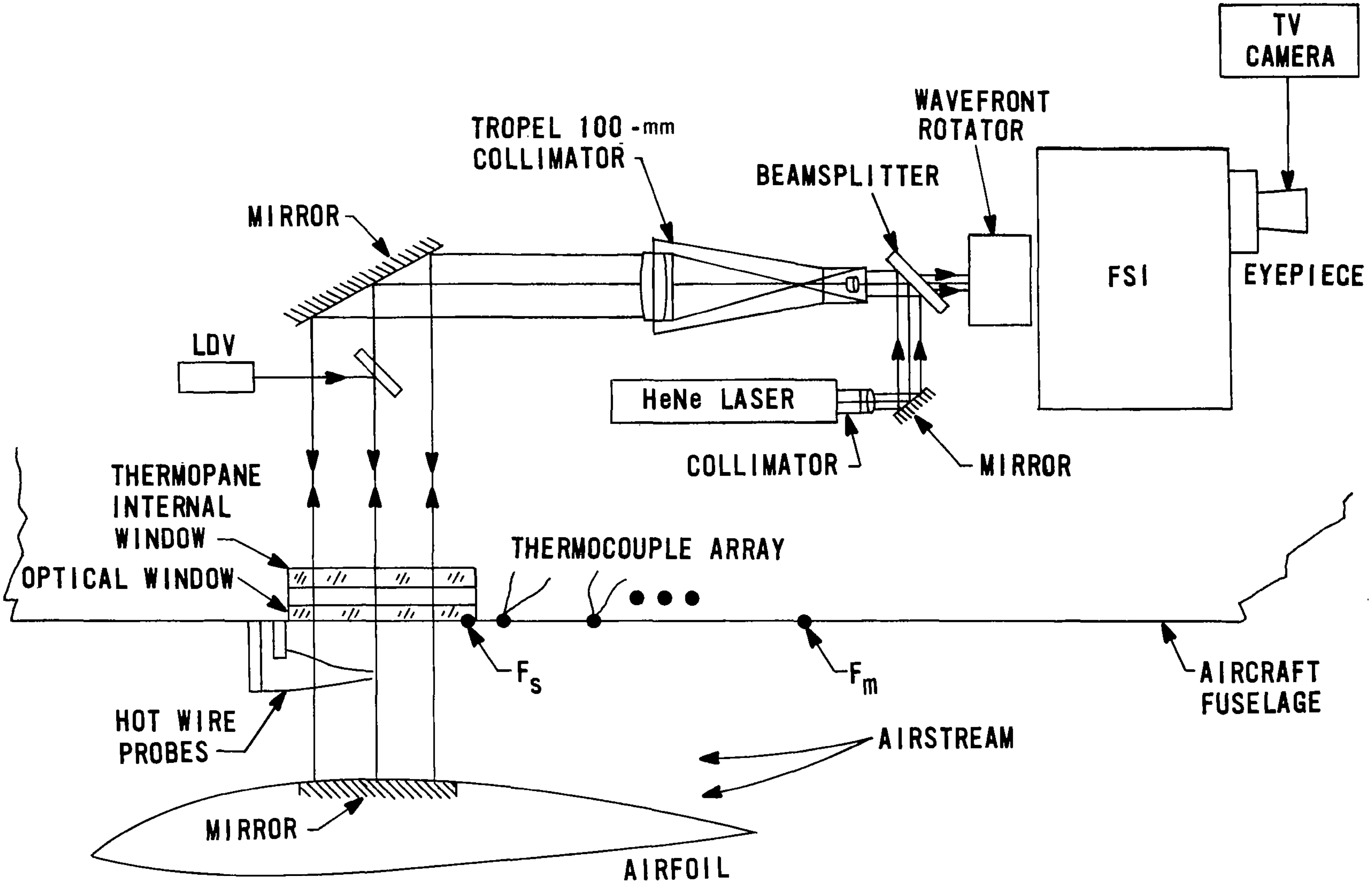

Fig. 1a Schematic for KC-135 Aero-Optical Experimental Setup.

Fig. 1b Hardware for KC-135 Aero-Optical Experimental Setup.

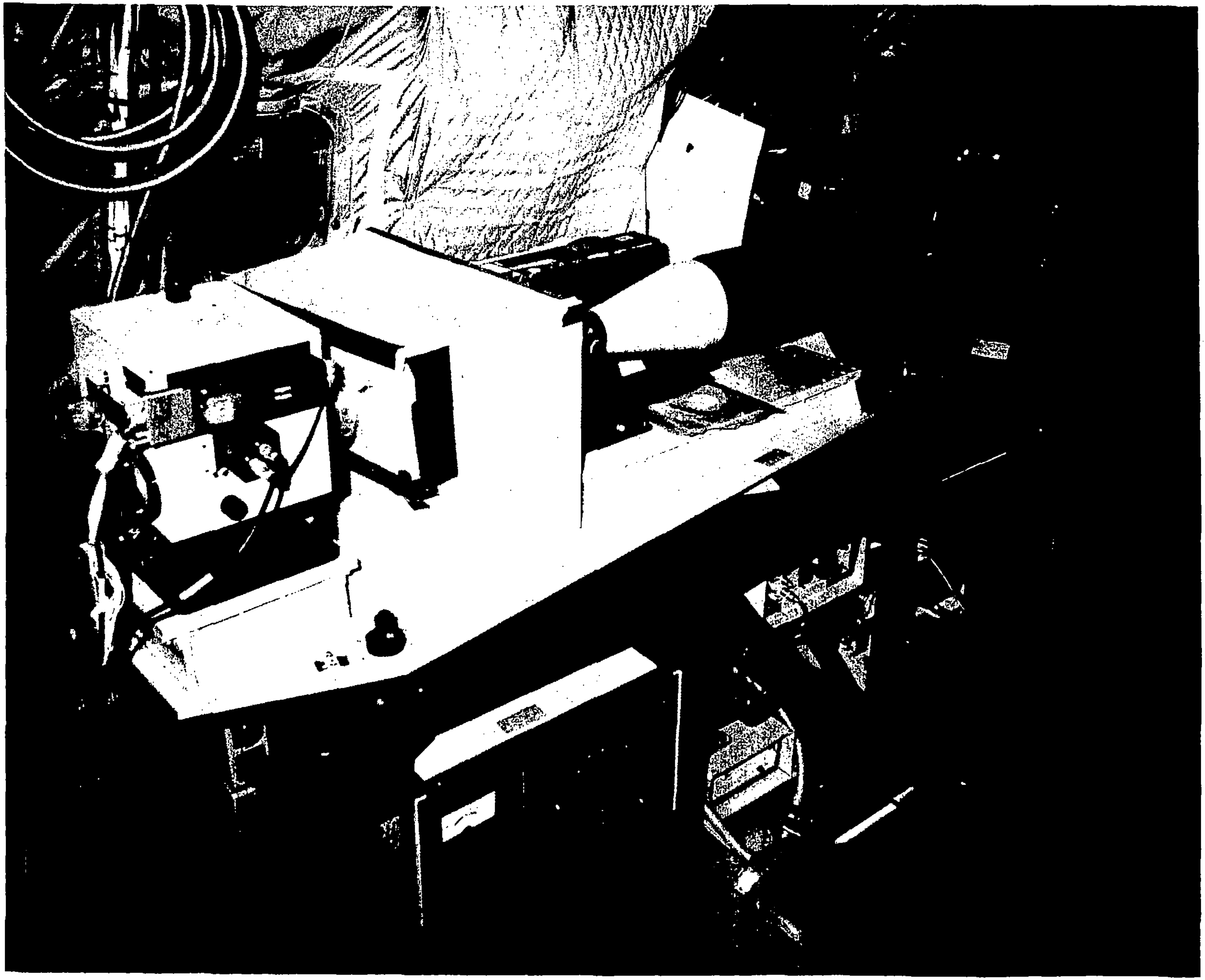

Fig. 1c Test bench for KC-135 Aero-Optical Experimental Setup.

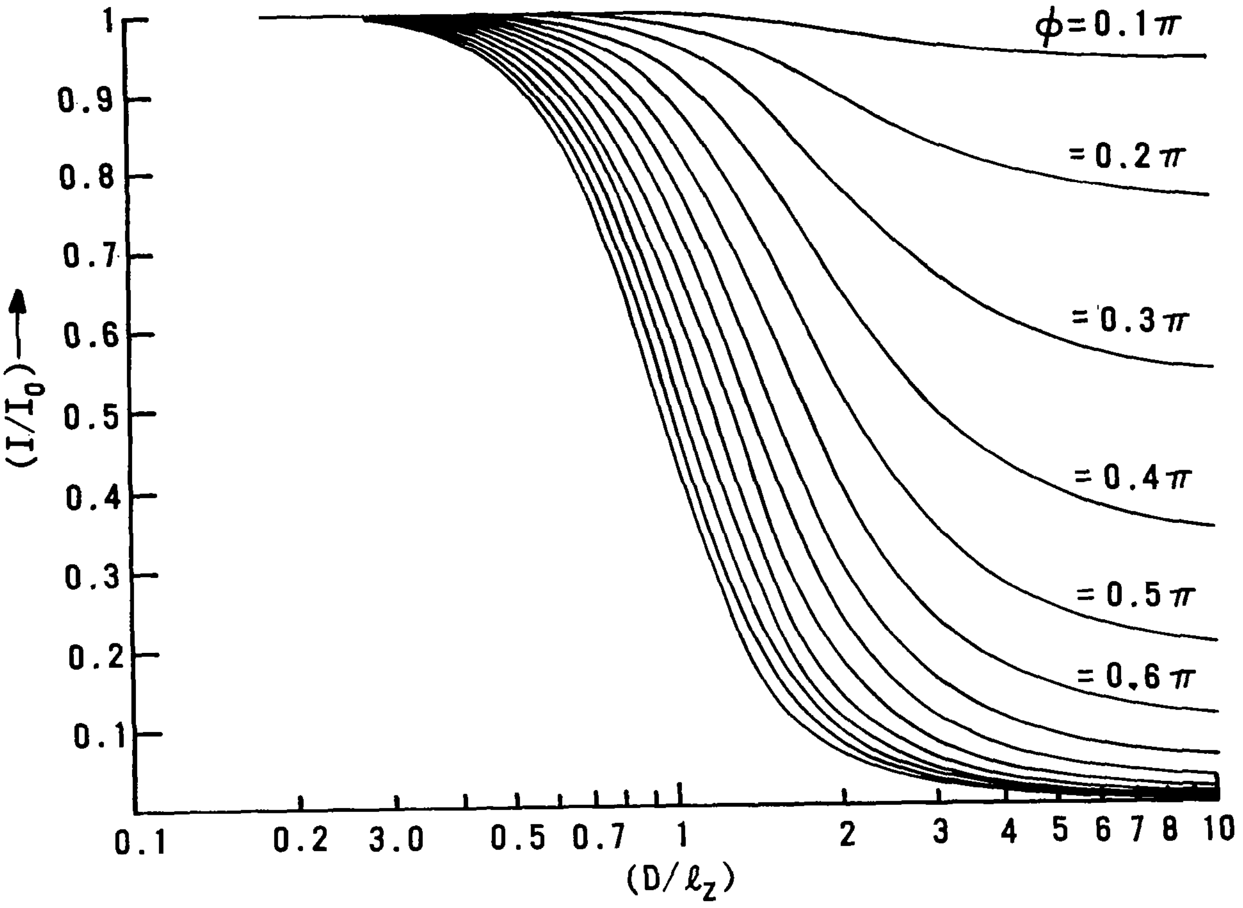

Fig. 2 Strehl family of I/I_0 Curves.

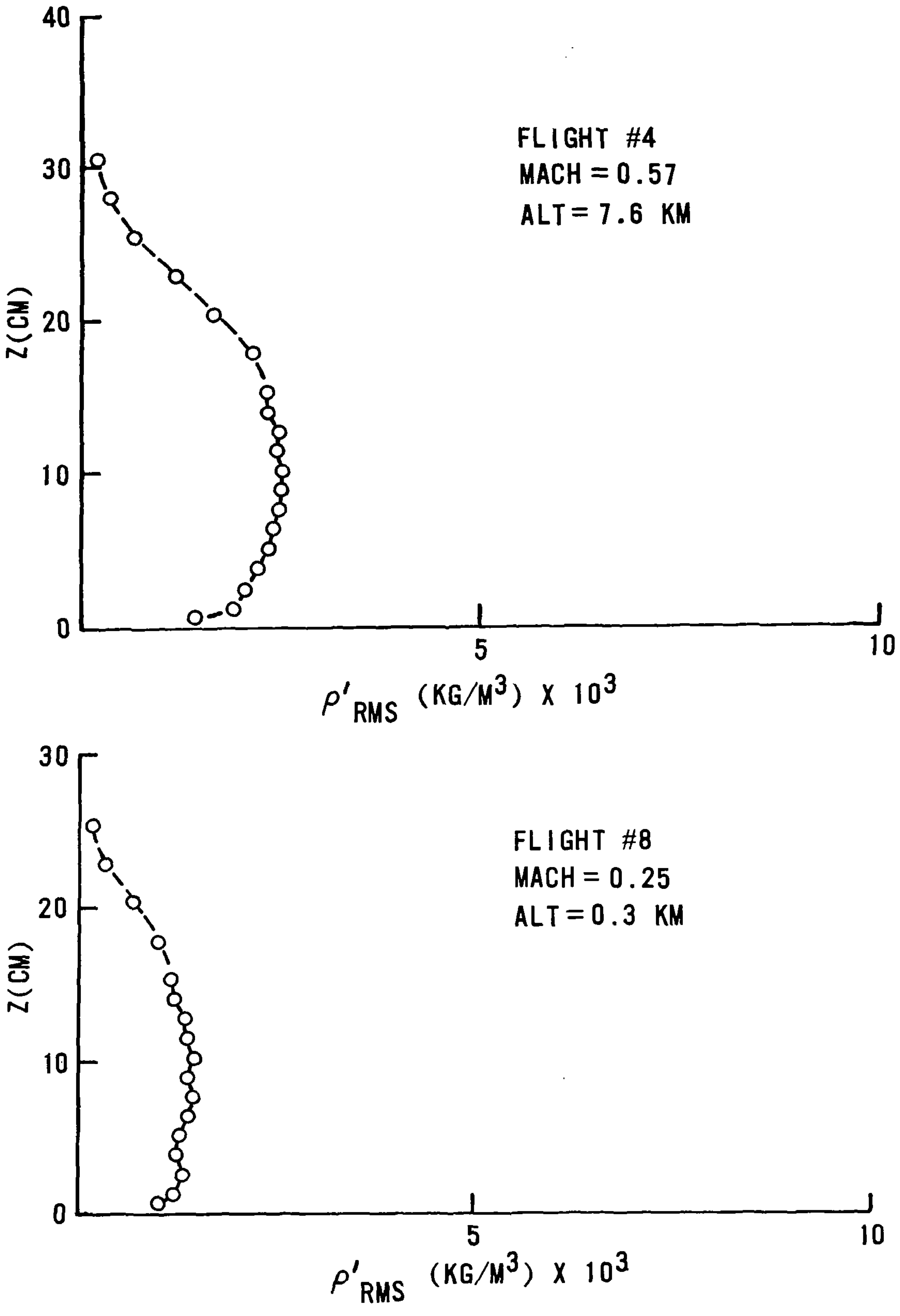

Fig. 3 Turbulent Boundary Layer Unsteady Density Profiles.

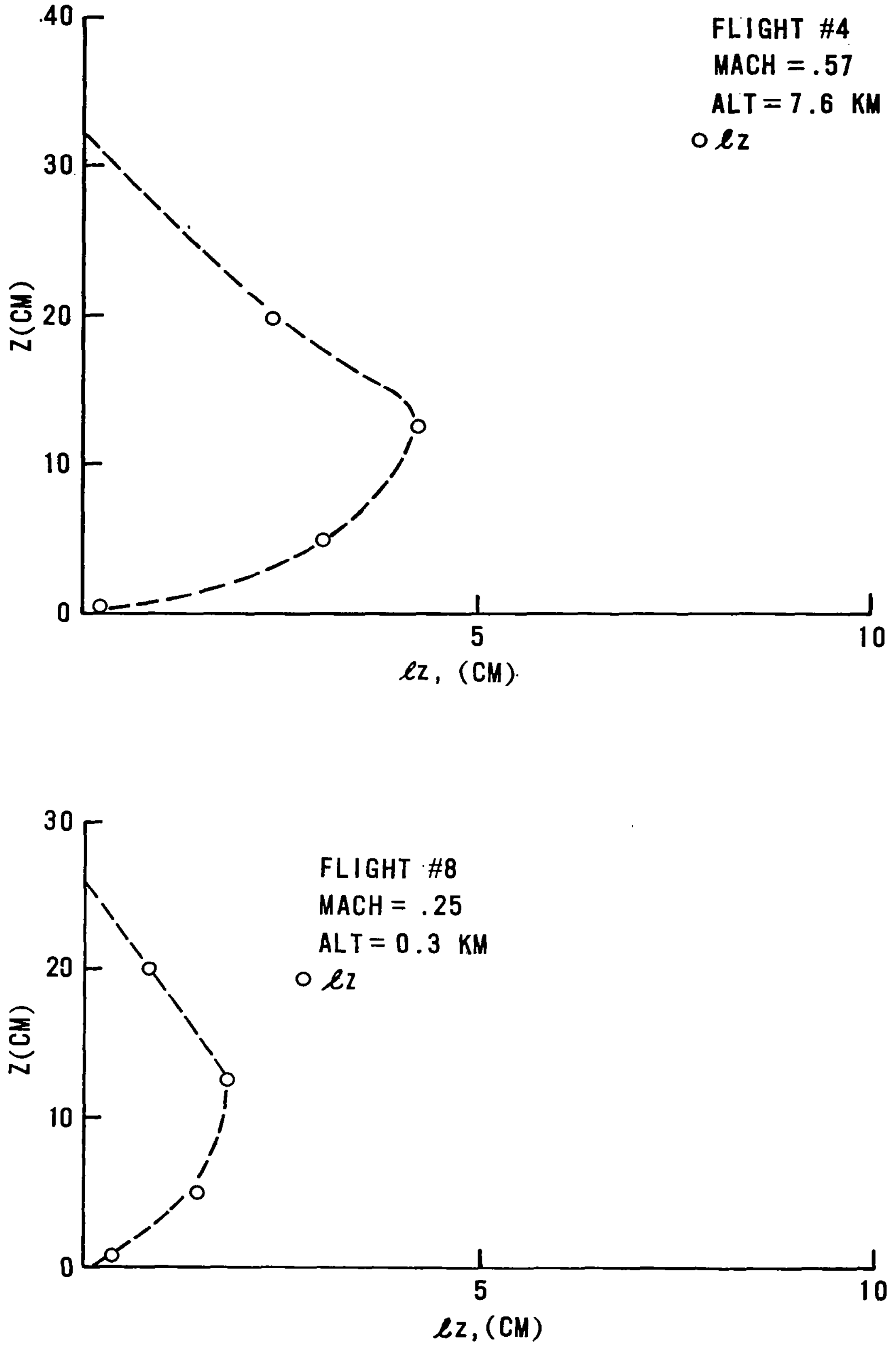

Fig. 4 Turbulent Boundary Layer Correlation Length Profiles.

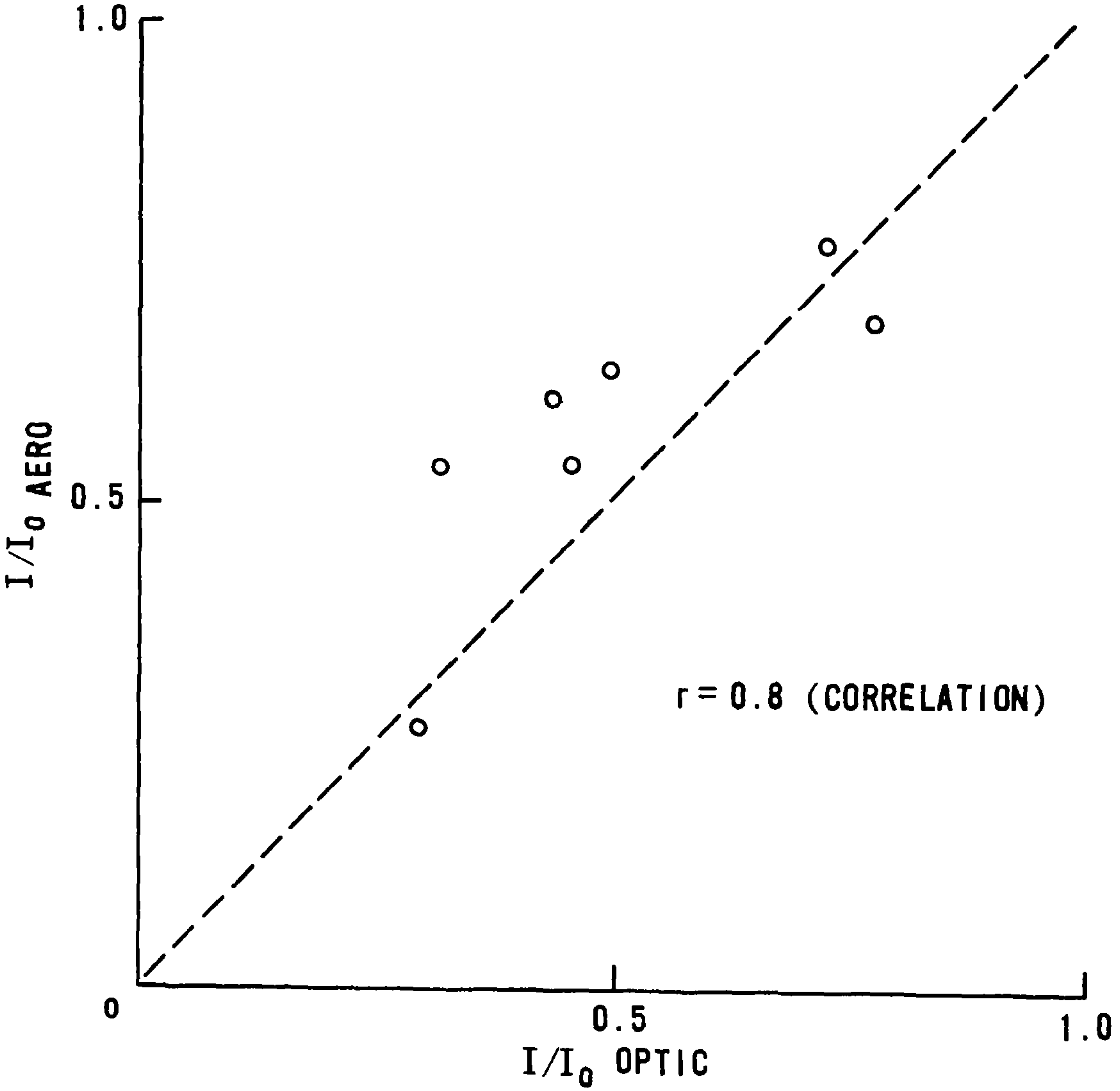

Fig. 5 Turbulent Boundary Layer Correlation Plot: Aerodynamic versus Optical Strehl Ratios.

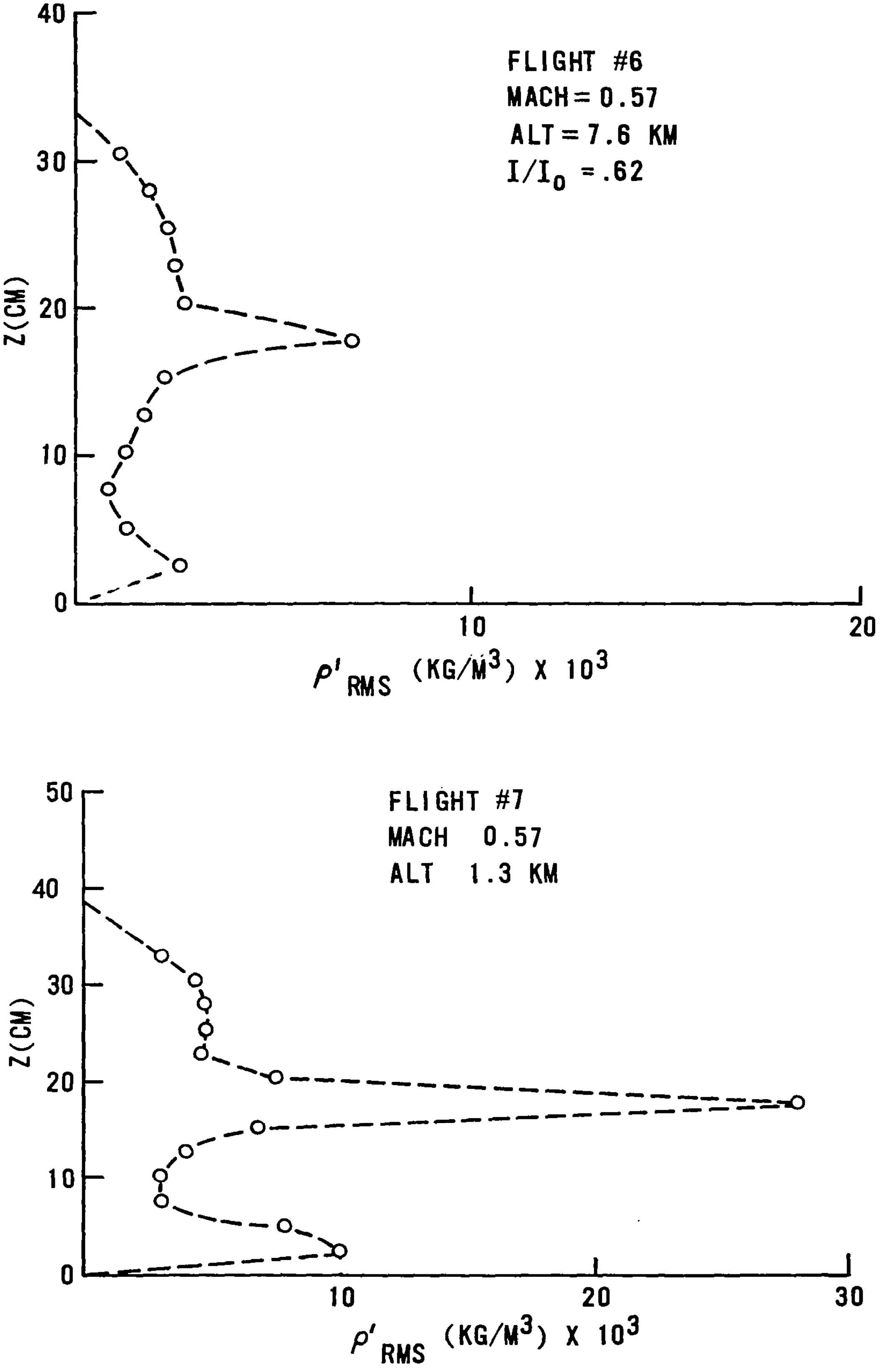

Fig. 6 Shear Layer Unsteady Density Profile.

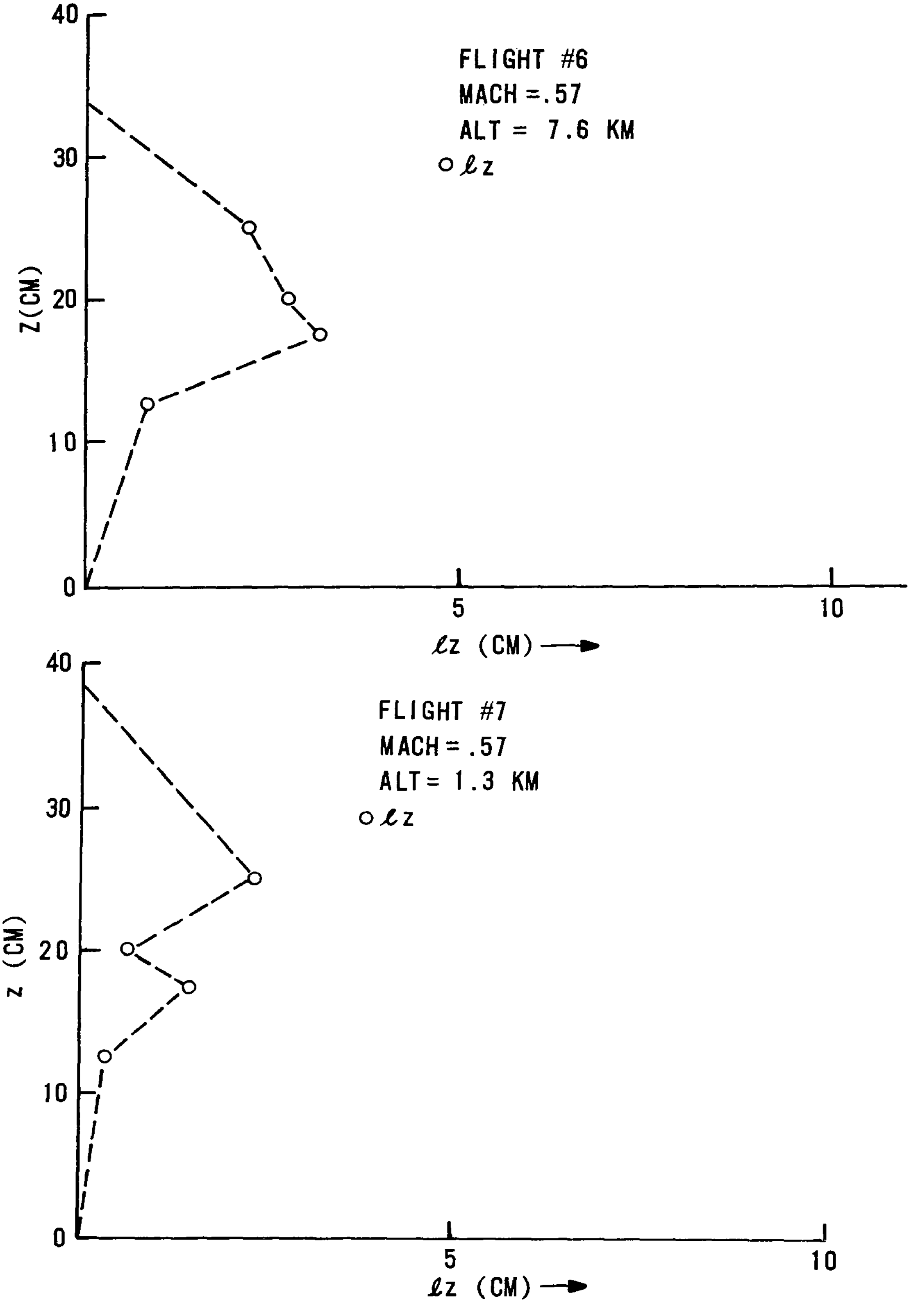

Fig. 7 Shear Layer Correlation Length Profiles.

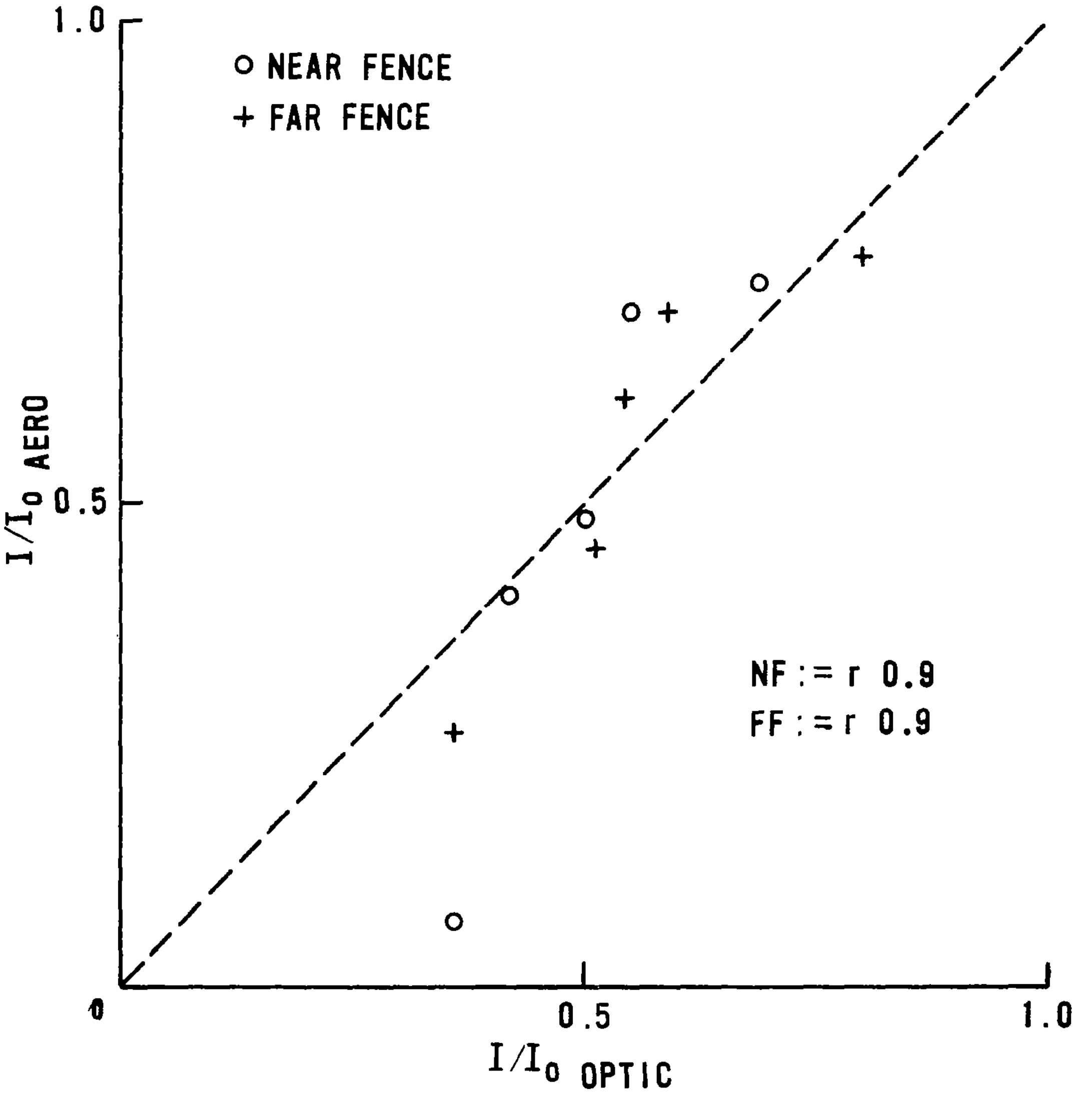

Fig. 8 Shear Layer Correlation Plot: Aerodynamic versus Optical Strehl Ratios.

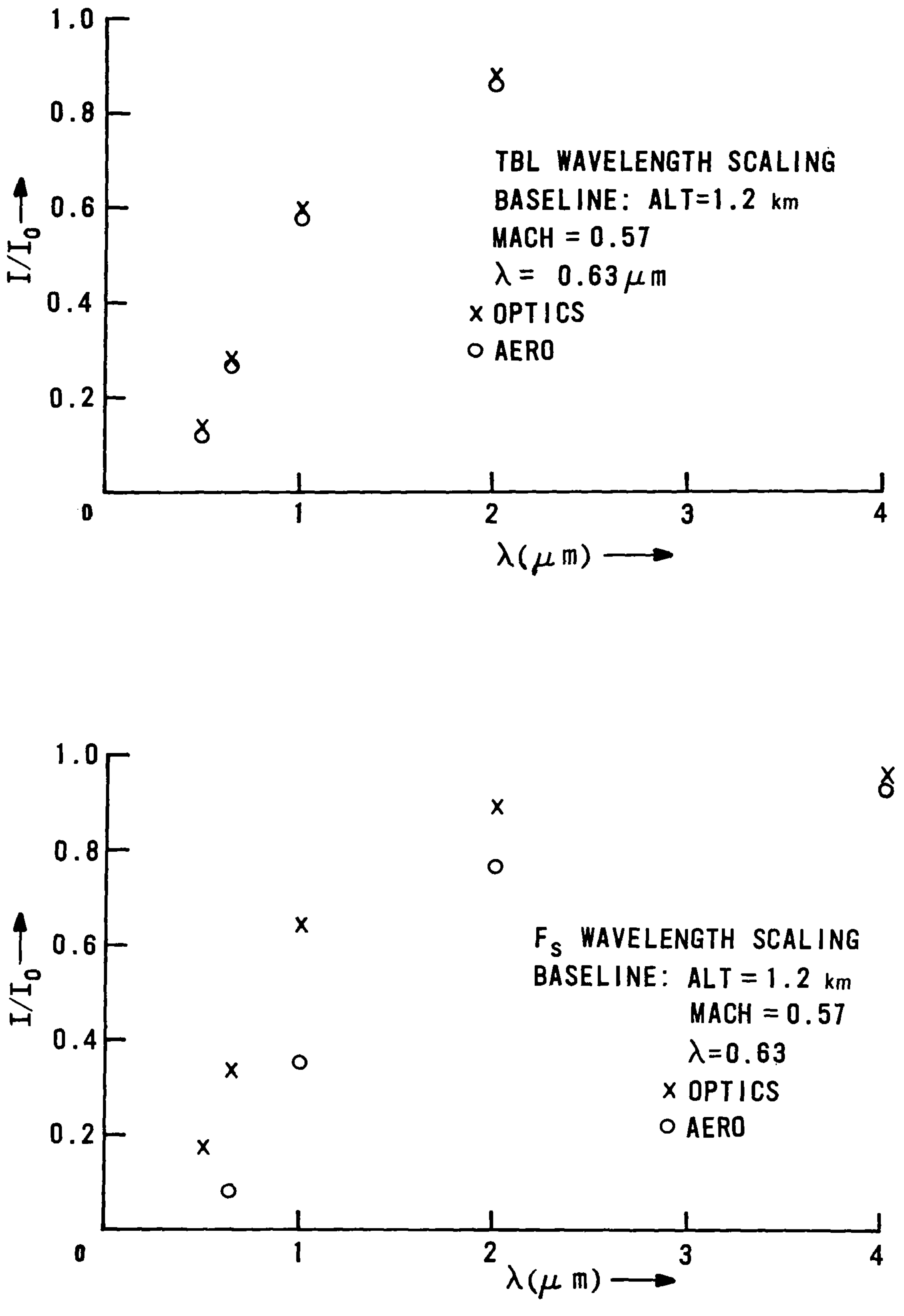

Fig. 9 Wavelength Scaling of Strehl Ratio I/I_0.

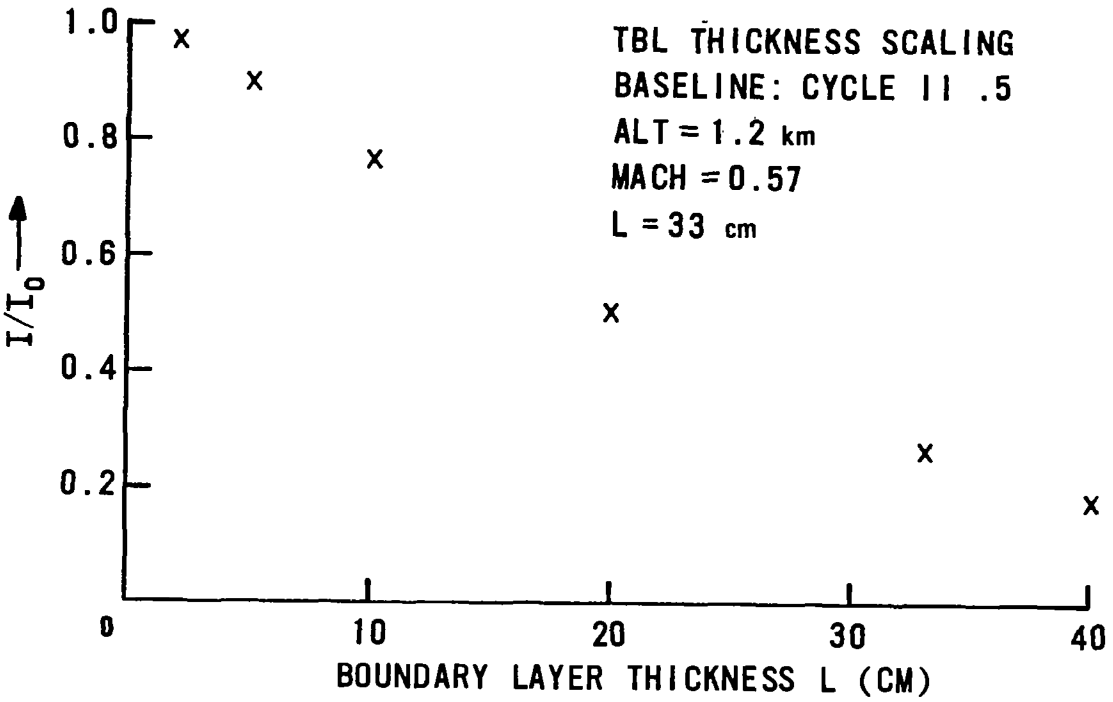

Fig. 10 Turbulent Boundary Layer Thickness Scaling of Strehl Ratio I/I_o.

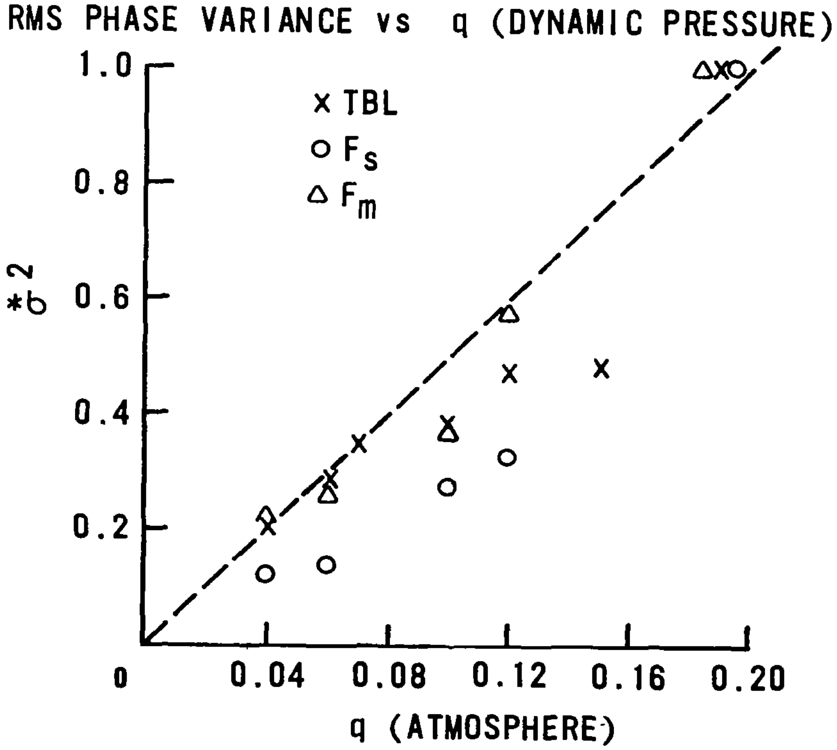

Fig. 11 Optical Phase Variance Scaling with Aircraft Dynamic Pressure (q).